A Computational Model for False Lumen Thrombosis in Type B Aortic Dissection Following Thoracic Endovascular Repair

Claudia Menichini[1], Zhuo Cheng[1], Richard G.J. Gibbs[2], Xiao Yun Xu[1]

[1]Department of Chemical Engineering, Imperial College London, London SW7 2AZ, UK

[2]Vascular Surgical Unit, St. Mary's Hospital, Imperial College Healthcare NHS Trust, London W2 1NY, UK

Word Count: 3600 words

Correspondence:
Professor Xiao Yun Xu
Department of Chemical Engineering
Imperial College London,
London SW7 2AZ, UK
+44 (0)20 7594 5588
Email: yun.xu@imperial.ac.uk

Abstract

Thoracic endovascular repair (TEVAR) has recently been established as the preferred treatment option for complicated type B dissection. This procedure involves covering the primary entry tear to stimulate aortic remodelling and promote false lumen thrombosis thereby restoring true lumen flow. However, complications associated with incomplete false lumen thrombosis, such as aortic dilatation and stent graft induced new entry tears, can arise after TEVAR. This study presents the application and validation of a recently developed mathematical model for patient-specific prediction of thrombus formation and growth under physiologically realistic flow conditions. The model predicts thrombosis through the evaluation of shear rates, fluid residence time and platelet distribution, based on convection-diffusion-reaction transport equations. The model was applied to 3 type B aortic dissection patients: two TEVAR cases showing complete and incomplete false lumen thrombosis respectively, and one medically treated dissection with no signs of thrombosis. Predicted thrombus growth over time was validated against follow-up CT scans, showing good agreement with *in vivo* data in all cases with a maximum difference between predicted and measured false lumen reduction below 8%. Our results demonstrate that TEVAR-induced thrombus formation in type B aortic dissection can be predicted based on patient-specific anatomy and physiologically realistic boundary conditions. Our model can be used to identify anatomical or stent graft related factors that are associated with incomplete false lumen thrombosis following TEVAR, which may help clinicians develop personalised treatment plans for dissection patients in the future.

Keywords: CFD, Aortic dissection, TEVAR, Thrombosis, False lumen, Hemodynamics

Word Count: 237/250

1. Introduction

Thoracic endovascular aortic repair (TEVAR) has been recently established as a viable alternative to open surgery for complicated acute type B distal dissections (Hanna et al., 2014), and has shown promising results for the treatment of both acute and chronic uncomplicated cases (Nienaber et al., 2014; Brunkwall et al., 2014). This minimally invasive procedure involves the placement of an endovascular stent-graft in order to seal the primary entry tear in the hope of reducing pressure in the false lumen (FL), promoting remodelling of the aorta, and inducing complete FL thrombosis, thereby restoring aortic flow. However, complete FL thrombosis is not always achieved. Risk factors such as the presence of distal re-entry tears and visceral vessels arising from the FL can lead to retrograde flow along the stent graft and perpetuate FL flow resulting in incomplete thrombosis (Qin et al., 2012). The latter has been associated with higher mortality rates due to increases in FL mean and diastolic pressure, causing further complications, such as aortic expansion and the formation of stent graft-induced new entry tears (Dong et al., 2010). It is therefore important to understand the hemodynamic and biomechanical consequences of TEVAR and what stent-graft designs and aortic morphologies would favour complete FL thrombosis.

The evaluation of hemodynamic parameters and their links with anatomical features plays an important role in understanding pathogenesis and evolution of vascular diseases and in improving treatment outcomes. In the last decade, computational fluid dynamics (CFD) studies have provided better insights into the hemodynamic environment associated with aortic dissection (AD), and have allowed the estimation of parameters such as wall shear stress (WSS) and pressure, which are difficult to measure *in vivo* (Sun and Chaichana, 2016;

Doyle and Norman, 2016). CFD studies have demonstrated that flow in AD is disturbed, with a high velocity jet through the primary entry tear, strong recirculation in the FL and near the tears and large variations in WSS (Tse et al., 2011; Chen et al., 2013; Alimohammadi et al., 2014; Cheng et al., 2013; Wan Ab Naim et al.; 2014, Dillon-Murphy et al., 2015; Ahmed et al., 2016). Several authors have compared flow in pre and post-TEVAR aortas, in order to investigate its effect on AD hemodynamics (Karmonik et al., 2010; Midulla et al., 2012; Cheng et al., 2015; Sun and Chaichana, 2016), and a recent study by Nauta et al. (2017) focused on the influence of disturbed flow on the development of thrombus by evaluating platelet activation potential. Although these computational studies have provided valuable insights, little has been done to date to show directly how disturbed flow may lead to the growth of thrombus in the FL, in particular following TEVAR.

In this paper we present the application of a recently developed computational model to three AD cases in order to determine the model's capability to predict thrombus formation under realistic anatomical and flow conditions. The model has been previously tested on idealised AD geometries and validated against experimental data (Menichini and Xu, 2016). It has also been applied to realistic AD geometries based on patient-specific anatomical data, showing good qualitative agreement between the predicted thrombus growth pattern and *in vivo* observations at multiple follow-up stages (Menichini et al., 2016). Here, we further extend the model to patient-specific studies following TEVAR, and evaluate its predictive capability by qualitative and quantitative comparisons with *in vivo* data.

2. Methods

Two patient-specific post-TEVAR models were included: (i) one for a patient who developed complete FL thrombosis following TEVAR (TEVAR-P1), (ii) one for a patient who developed partial FL thrombosis (TEVAR-P2). Both patients were classified as complicated, and were treated with TEVAR in acute phase. Patient TEVAR-P1 was treated with a Gore TAG device (W. L. Gore & Associates, Flagstaff, Arizona; proximal diameter: 31 mm, distal diameter: 31 mm, endoprosthesis length: 20 cm), while patient TEVAR-P2 was treated with a Medtronic Valiant Captivia device (Medtronic/AVE, Minneapolis, Minnesota; proximal diameter: 34 mm, distal diameter: 34 mm, endoprosthesis length: 20 cm). A third uncomplicated patient who was under medical treatment and did not show any signs of FL thrombosis during follow-up was also included as a benchmark case (BMT). All patients were kept under CT surveillance. Formal ethical approval was not required for this retrospective study, as prior agreement was made to undertake computational modelling work using totally anonymised images without requiring further specific ethics committee agreement for individual patients. All data were analysed anonymously and patient information was de-identified prior to analysis.

The post-TEVAR models were reconstructed using Mimics (Materialize HQ, Leuven) from CT images acquired within one month after TEVAR. All CT scans were performed with a Philips Mx8000 IDT 16 scanner, with voxel sizes in the range of (0.75-0.92) x (0.75-0.92) x 2 mm^3 and FoVs between 382-477 mm. As the focus of this study was to predict thrombosis within the FL, all branches were excluded from the analysis. The models were meshed using ICEM 15 (Ansys Inc.), and mesh sensitivity tests were performed to ensure mesh independence for each case. As the growth of thrombus is driven by hemodynamic parameters, the sensitivity test was focused on ensuring mesh independence of the flow field. Three meshes

were tested for each geometric model, and differences in peak wall shear stress and velocity below 2% were considered acceptable. The final grids represented a compromise between accuracy and computational cost and comprised approximately 3 million elements each, with a tetrahedral core and 10 prismatic layers near the walls. A fine resolution in the boundary layer is essential to guarantee accuracy in WSS predictions and smooth thrombus propagation. Larger element size was used in the core region, while gradual changes were made to avoid sudden jump in mesh size, which could compromise thrombus growth patterns.

Thrombus formation was simulated using the hemodynamics-based model developed by Menichini and Xu (2016) and modified by Menichini et al. (2016). The computational model identifies regions of thrombus growth through the evaluation of time-averaged WSS and shear rates, as well as the distribution of activated and resting platelets and fluid residence time. The growth of thrombus is tracked through the local concentration of a species denoted as bound platelets (BP), which is used as a surrogate for thrombus. Thrombus growth is predicted through a feedback mechanism which controls the formation of thrombus by allowing BP to accumulate in regions of high concentration of activated platelets, low shear and long residence times, and by stopping thrombus growth when these conditions are not satisfied. The full set of equations for the thrombus growth model and all model parameters can be found in the Appendix. As in our previous studies, the rate of thrombus growth was artificially accelerated in order to allow predictions to be obtained in a feasible time frame (Menichini and Xu, 2016).

The patient-specific models were implemented in Ansys CFX 15 with a high-resolution spatial discretisation scheme. Blood was treated as a non-Newtonian fluid described by the Quemada model (Quemada, 1978) and the flow was assumed to be laminar. A realistic flow waveform extracted from the literature (Cheng et al., 2014) was applied at the inlet of each model with a flat velocity profile. This boundary condition was deemed appropriate as our region of interest is located distal to the aortic arch (Cheng et al, 2014). Realistic 3D inlet velocity profiles would be needed for faithful prediction of flow in the ascending aorta, but these were found to have a negligible effect on flow in the descending aorta (Morbiducci et al., 2013). The walls were assumed to be rigid with no slip conditions. The flow split between the iliac arteries in the two post-TEVAR models was regulated by a 3-element Windkessel model (3EWM) outlet boundary condition (Dillon-Murphy et al., 2015), which describes the relationship between pressure and flowrate based on the analogy between electrical circuits and the cardiovascular system (Ruel and Lachance, 2010). For the BMT model, a pressure waveform calculated through a 3EWM was applied at the only outlet. Values for the 3EWM parameters were extracted from the literature (Xiao et al., 2014), as no patient-specific data was available. The boundary conditions applied in the three models are summarised in Fig. 1, with the respective outlet flows derived from the 3EWM. A fixed time-step of 0.005 s was adopted based on previous time-step sensitivity test (Menichini and Xu, 2016) and numerical simulations were carried out until thrombus growth stopped, which occurred after 20 cardiac cycles for TEVAR-P1, 42 cycles for TEVAR-P2, and 10 cycles for BMT. Simulation results were post-processed using CEI Ensight 10 and predictions of thrombus growth over time were validated against follow-up data.

3. Results

143 *3.1 Model Geometries*

144 Fig. 2 shows the reconstructed geometries based on initial CT scans for all three patients
145 together with the stent graft coverage for the TEVAR cases. In TEVAR-P1, the stent graft
146 starts from below the left subclavian artery and covers the entire thoracic aorta and part of
147 the abdominal aorta up to the celiac artery. Below the stented region, only one re-entry tear
148 is observed, which has an area of around 20 mm^2 and is located at the iliac bifurcation level.
149 The remaining FL extends upwards towards the celiac artery and downwards towards the
150 iliac bifurcation. TEVAR-P2 presents a different stent configuration, with the stent graft
151 covering the left subclavian artery and having a shorter length limited to the thoracic aorta.
152 Several small re-entry tears are observed below the stented region at the celiac and renal
153 levels, with respective areas of 15.5 mm^2 and 20.5 mm^2, and two larger tears at the iliac
154 bifurcation level, with respective areas of 44.5 mm^2 and 95 mm^2. In the BMT patient the FL
155 extends upwards reaching the top of the aortic arch and downwards to the celiac artery.
156 Two main tears can be observed, one is located on the outer curve of the aortic arch with an
157 area of 192 mm^2, and another right above the celiac artery with a 124 mm^2 area. In all
158 models, smaller tears could not be measured due to the limited image resolution, and all
159 the measurements taken were subject to uncertainty determined by the voxel size.

160

161 *3.2 Flow Patterns and Wall Shear Stress*

162 Instantaneous streamlines at three time points of the cardiac cycle are shown in Fig. 3 for all
163 three patients. For TEVAR-P1, particularly low velocities are observed in the FL, with slow
164 flow recirculation in the tear region and almost static flow in the entire FL at all phases of
165 the cardiac cycle. Extended recirculation areas exist in the FL for TEVAR-P2 where the
166 presence of multiple distal tears allows for flow recirculation in between the tears. For this

patient, high velocities are observed in proximity of the tears during systole (Fig. 3a and b), while highly disturbed flow patterns are observed in the FL during mid-deceleration and diastolic phase (Fig. 3c) as the distal tears allow blood to alternatively enter or exit the FL.

The different morphological features of the BMT model, characterised by an open entry tear located in the distal aortic arch and larger tear areas, are reflected in different flow patterns. High velocities are observed near the entry tear at all times with a larger volume of blood entering the FL, and flow recirculation is observed in the top FL region. The large distance between the tears in this case allows the flow to become more developed in the FL than in TEVAR-P2, with well organised flow patterns in the region in between the tears during systolic acceleration. Disturbed flow patterns are observed in the FL in mid-deceleration and diastolic phase, when the two tears invert their roles as entry to and exit of the FL.

The aforementioned flow patterns dictate the distribution of time-averaged WSS (TAWSS) (Fig. 4). Very low TAWSS is observed in the entire FL in TEVAR-P1. For TEVAR-P2, the flow jets passing through the uncovered re-entry tears cause increases in local TAWSS on the opposite wall, whereas TAWSS in the rest of the FL is low, with particularly low values in the top FL region and in-between the tears, corresponding to areas of low velocities and flow recirculation. In the BMT case, high TAWSS is observed near the entry and re-entry tears while lower values are seen in the region in-between the tears and at the top of the FL, but the magnitude of TAWSS is above 0.5 Pa.

3.3 Thrombus Growth

Predicted thrombus growth patterns were compared with follow-up clinical data. For TEVAR-P1, thrombus started forming on the FL walls and expanded uniformly towards the centre of the FL (Fig. 5). As the thrombus approached the distal tear, the growth rate was significantly reduced and eventually stopped after approximately 15 s, at which point the FL was completely thrombosed. As no further change was predicted thereafter, the simulation was stopped at 20 s. These results compare well with clinical follow-ups showing complete thrombosis of the FL after approximately four months following TEVAR.

For TEVAR-P2, thrombus formation started from the top FL (Fig. 6a and 6b) and gradually expanded towards the first tear. At 20 s (Fig. 6c) almost all the FL above the first tear was thrombosed. At some point between 8-20 s, thrombus started to form in-between the first and second tears, which grew very slowly until at 40 s (Fig. 6d) when no further change could be predicted. Comparing the FL volume at 40 s with its initial volume indicated a predicted FL volume reduction of 93.8%. These results were compared with *in vivo* measurements from the follow-up scans. The first follow-up at 1 year (Fig. 6e) showed partial thrombosis in the top FL region, which was well captured by the simulation result shown in Fig.6b. After 4 years the top FL region was completely thrombosed (Fig. 6f), while the area in-between the tears remained partially patent, with a measured FL volume reduction of 86.2% over the entire follow-up period.

The thrombosis model was also used to simulate thrombus formation in the BMT case. A periodic flow solution was obtained after 3 cardiac cycles, and no thrombus formation was predicted over 10 cycles, after which the simulation was stopped as the results would not

change anymore. The predicted outcome of no FL thrombosis in this case is consistent with the corresponding follow-up data.

4. Discussion

The extent of FL thrombosis has been identified as a key parameter to evaluate endovascular and medical treatment outcomes for aortic dissection (Tsai et al., 2007; Trimarchi et al., 2013). The use of a computational model to predict FL thrombosis could help identify which anatomical features and stent-graft related factors would favour complete FL thrombosis. This information could potentially be used to guide initial treatment plans and improve stent graft design.

We have developed an efficient computational model for the prediction of thrombus growth over time through the evaluation of blood flow patterns and hemodynamic parameters (Menichini and Xu, 2016; Menichini et al., 2016). This model allows us to predict which regions of the FL are most likely to be thrombosed and how this would affect blood flow patterns and hence further growth of thrombus. The present study is an extension of our previous work by testing the model's capability of predicting device-induced FL thrombosis after TEVAR. A medically treated patient showing no thrombosis was included for benchmarking.

The results demonstrate that our computational model is capable of predicting both spontaneous and device-induced thrombosis. In TEVAR-P1, complete FL thrombosis was predicted within a simulation time of 15 cardiac cycles. Thrombosis started from the FL walls and expanded rapidly in the initial stage, which was followed by a period of slow growth

until thrombi reached the uncovered tear when thrombosis eventually stopped. In TEVAR-P2, thrombus formation was initially observed in the top FL region with a rapid growth rate, but its growth slowed down dramatically as the thrombus propagated towards the first uncovered tear. Thrombus formation in the upper FL caused a significant reduction in TAWSS in the region in-between the two tears, initiating partial thrombosis in this area. These findings are consistent with clinical studies which show that the presence of distal tears and branching vessels arising from the FL are risk factors for incomplete FL thrombosis (Clough and Nienaber, 2015; Qin et al., 2012; Kamman et al., 2016). Similar results were also observed in our previous study, where the formation of a second tear in a medically treated patient caused lateral thrombosis in the region in-between the tears (Menichini et al., 2016). However, the BMT case included in the present study showed no sign of thrombosis in our computational prediction or follow-up scans, even though a distal tear is present in the descending aorta. This was possibly due to the relatively large distance between the two tears, which helped reduce the level of flow disturbance in the FL. The organised flow patterns produced TAWSS in the normal physiological range, thereby preventing the formation of thrombi. These results suggest that the distance between tears may be an important factor in determining FL thrombosis, although more cases will be needed to elucidate its role. Additionally, contrary to TEVAR-P1 and TEVAR-P2, the BMT case showed no FL thrombosis in the top FL region. As the BMT patient presented a much shorter retrograde expansion in the upper FL as compared to the TEVAR patients studied, it is plausible to speculate that the distance between the primary entry tear and the top of the FL could be an important determinant of FL thrombosis in the proximal region.

Limitations in computational power and data storage space currently hinder the simulation of real-time thrombosis on the true time scale of months or even years typical of FL thrombosis in aortic dissection (Malaspinas et al., 2016). Our strategy is to use a computationally efficient model that is capable of providing fast and reliable predictions of thrombus formation and growth, with a view to identifying anatomical or stent graft related factors that may promote complete FL thrombosis after TEVAR. The use of accelerated kinetics allows us to predict growth patterns and final outcomes, without simulating the real-time evolution of thrombi. For TEVAR-P1, complete thrombosis was observed four months after TEVAR and the simulation of 15 cardiac cycles was sufficient to reproduce clinical observations. A much longer simulation time was required to reproduce the *in vivo* results observed on TEVAR-P2 at four-year follow-up. It may be possible that a relationship exists between the simulated time-scale and the effective growth rate. As many environmental and patient-specific factors are likely to affect the time scale of thrombus growth in each patient, only the analysis of a large cohort of patients will allow us to explore the possibility of finding a scale factor between our simulated time and real time thrombosis.

This work is presented as a pilot study to demonstrate the potential applicability of our model to the prediction of thrombosis following TEVAR. In order to minimize computational costs, the model geometries adopted here do not include the arch and visceral branches. This choice is partially due to the lack of patient-specific flow and pressure information, which hinders the calibration of additional Windkessel models. The study carried out by Cheng et al. (2014) showed satisfactory agreement between simulation results and velocities measured with phase-contrast MRI, demonstrating that the exclusion of arch

branches had a minor effect on flow in the proximal descending aorta in type B AD. However, the influence of visceral branches is unclear and it appears that their exclusion may have resulted in an over-prediction of the iliac flow in TEVAR-P2, where the celiac and one of the renal arteries arise from the FL. This may be responsible for the ~8% difference in FL thrombus volume between our predictions and *in vivo* data for this patient. As there are no side branches arising from the FL in the TEVAR-P1 and BMT cases, no obvious differences were found between the predicted and observed patterns of thrombosis. While in this study it seems that the exclusion of visceral branches had only a minor effect due to their specific locations, dissection geometries can vary considerably from patient to patient, and in cases where multiple branches are attached to the FL, their effects could be significant. Future work will address the effects of visceral branches and compliant walls so as to improve the accuracy of predicted thrombus formation and growth, and to provide physiologically realistic pressure within the FL; the latter is required to predict potential future complications, such as aortic expansion or the formation of new entry tears.

Once fully validated, the model will be applied to a large cohort of patients in order to identify which parameters have the strongest effect on thrombus formation. These findings will hopefully help surgeons to more consciously select their treatment strategy. Our long term objective is to develop a powerful decision making tool to determine optimal treatments for each patient. However, at the current stage of research these computations are intensely time-consuming, which will be a major barrier for the intended clinical application. Hence, more efforts are needed to further improve the computational efficiency of the thrombosis model.

5. Conclusion

In this paper we have presented the application of a hemodynamics-based model to the study of FL thrombosis in three patient-specific cases of type B aortic dissection, showing complete, partial and no thrombosis, respectively. In all three cases, the model was able to predict the same outcome and thrombus growth patterns as observed *in vivo*, demonstrating its applicability to the study of both spontaneous and device-induced thrombosis in aortic dissection. It is hoped that our model can be used to identify anatomical or stent-graft related factors that are associated with incomplete false lumen thrombosis following TEVAR, which may help clinicians develop personalised treatment plans for dissection patients in the future.

Acknowledgement

This project is funded by a PhD scholarship awarded to CM by the Department of Chemical Engineering at Imperial College London and by Imperial College Healthcare Charity.

Conflict of interest statement

The authors have no conflict of interest to declare.

References

Ahmed, S.B., Dillon-Murphy, D., Figueroa, C.A., 2016. Computational Study of anatomical risk factors in idealized models of type B aortic dissection. European Journal of Vascular and Endovascular Surgery 52(6), 736-745.

Alimohammadi, M., Agu, O., Balabani, S., Díaz-Zuccarini, V., 2014. Development of a patient-specific simulation tool to analyse aortic dissections: assessment of mixed patient-specific flow and pressure boundary conditions. Medical engineering & physics 36(3), 275-284.

Alimohammadi, M., Pichardo-Almarza, C., Agu, O.,Díaz-Zuccarini, V., 2016. Development of a patient-specific multi-scale model to understand atherosclerosis and calcification locations: comparison with in vivo data in an aortic dissection. Frontiers in Physiology 7.

Anand M., Rajagopal K., Rajagopal K.R., 2003. A model incorporating some of the mechanical and biochemical factors underlying clot formation and dissolution in flowing blood. J Theor Med 5, 183–218.

Brunkwall J., Kasprzak P., Verhoeven E., Heijmen R., Taylor P., the ADSORB Trialists, 2014. Endovascular repair of acute uncomplicated aortic type B dissection promotes aortic remodelling: 1 year results of the ADSORB trial. Eur J Vasc Endovasc 48(3), 285-291.

Chen D., Müller-Eschner M., von Tengg-Kobligk H., Barber D., Böckler D., Hose R., Ventikos Y., 2013. A patient-specific study of type-B aortic dissection: evaluation of true-false lumen blood exchange. Biomedical engineering online, 12(1), 65.

Cheng Z., Juli C., Wood N.B., Gibbs R.G.J., Xu X.Y., 2014. Predicting flow in aortic dissection: comparison of computational model with PC-MRI velocity measurements. Med Eng Phys 36(9), 1176-1184.

Cheng Z., Riga C., Chan J., Hamady M., Wood N.B., Cheshire N.J., Xu X.Y., Gibbs R.G., 2013. Initial findings and potential applicability of computational simulation of the aorta in acute type b dissection. J Vasc Surg 57, 35S–43S.

Cheng Z., Wood N.B., Gibbs R.G., Xu X.Y., 2015. Geometric and flow features of type B aortic dissection: initial findings and comparison of medically treated and stented cases. Ann Biomed Eng 43(1), 177-189.

355 Clough R.E., Nienaber C.A., 2015. Management of acute aortic syndrome. Nat Rev
356 Cardiol 12(2), 103-114.
357 Diamond S.L., 1999. Engineering design of optimal strategies for blood clot dissolution. Annu
358 Rev Biomed Eng 1, 427–461
359 Dillon-Murphy D., Noorani A., Nordsletten D., Figueroa A., 2015. Multi-modality image-
360 based computational analysis of haemodynamics in aortic dissection. Biomech Model
361 Mechan 15(4), 857-876.
362 Dong Z., Fu W., Wang Y., Wang C., Yan Z., Guo D., Xu X., Chen B., 2010. Stent graft-induced
363 new entry after endovascular repair for Stanford type B aortic dissection. Journal of vascular
364 surgery, 52(6), 1450-1457.
365 Doyle B.J., Norman P.E., 2016. Computational Biomechanics in Thoracic Aortic Dissection:
366 Today's Approaches and Tomorrow's Opportunities. Ann Biomed Eng 44(1), 71-83.
367 Ghirelli F., Leckner B., 2004. Transport equation for the local residence time of a fluid. Chem
368 Eng Sci 59, 513–523.
369 Hanna J.M., Andersen N.D., Ganapathi A.M., McCann R.L., Hughes G.C., 2014. Five-year
370 results for endovascular repair of acute complicated type B aortic dissection. J Vasc
371 Surg 9(1), 96-106.
372 Harrison S., Smith S., Bernsdorf J., Hose D., Lawford P., 2007. Application and validation of
373 the lattice boltzmann method for modelling flow-related clotting. J Biomech 40, 3023–3028.
374 Kamman, A.V., Brunkwall, J., Verhoeven, E.L., Heijmen, R.H., Trimarchi, S., 2017. Predictors
375 of aortic growth in uncomplicated type B aortic dissection from the Acute Dissection Stent
376 Grafting or Best Medical Treatment (ADSORB) database. Journal of Vascular Surgery 65(4),
377 964-971.

Karmonik C., Bismuth J., Davies M.G., Shah D.J., Younes H.K., Lumsden A.B., 2010. A computational fluid dynamics study pre-and post-stent graft placement in an acute type B aortic dissection. Vasc Endovascular Surg 45(2), 157-64

Malaspinas O., Turjman A., de Sousa D.R., Garcia-Cardena G., Raes M, Nguyen P.T.T., Zhang Y., Courbebaisse G, Lelubre C., Zouaoui Boudjeltia K., Chopard B., 2016. A spatio-temporal model for spontaneous thrombus formation in cerebral aneurysms. J Theor Biol 394, 68-76.

Menichini C., Cheng Z., Gibbs R.G.J., Xu X.Y., 2016. Predicting false lumen thrombosis in patient-specific models of aortic dissection, J R Soc Interface 13, 20160759.

Menichini C., Xu X.Y., 2016. Mathematical modeling of thrombus formation in idealized models of aortic dissection: initial findings and potential applications. J Math Biol 73(5), 1205-1226.

Midulla M., Moreno R., Baali A., Chau M., Negre-Salvayre A., Nicoud F., Pruvo J.P., Haulon S., Rousseau H., 2012. Haemodynamic imaging of thoracic stent-grafts by computational fluid dynamics (CFD): presentation of a patient-specific method combining magnetic resonance imaging and numerical simulations. Eur Radiol 22(10), 2094-2102.

Morbiducci U., Ponzini R., Gallo D., Bignardi C., Rizzo G., 2013. Inflow boundary conditions for image-based computational hemodynamics: impact of idealized versus measured velocity profiles in the human aorta. Journal of biomechanics, 46(1), 102-109.

Nauta, F. J., Lau, K. D., Arthurs, C. J., Eagle, K. A., Williams, D. M., Trimarchi, S., Himanshu, J.P., Figueroa, C.A., 2017. Computational Fluid Dynamics and Aortic Thrombus Formation Following Thoracic Endovascular Aortic Repair. The Annals of Thoracic Surgery.

Nesbitt W., Westein E., Tovar-Lopez F., Tolouei E., Mitchell A., Fu J., Carberry J., Fouras A., Jackson S., 2009. A shear gradient-dependent platelet aggregation mechanism drives thrombus formation. Nat Med 15, 665–673.

Nienaber C.A., Divchev D., Palisch H., Clough R.E., Richartz B., 2014. Early and late management of type B aortic dissection. Heart 100, 1491-1497.

Qin Y.L., Deng G., Li T.X., Jing R.W., Teng G.J., 2012. Risk factors of incomplete thrombosis in the false lumen after endovascular treatment of extensive acute type B aortic dissection. J Vasc Surgery 56(5), 1232-1238.

Quemada D., 1978. Rheology of concentrated disperse systems II. A model for non-newtonian Shear viscosity in steady flows. Rheol Acta 17(6), 632 -642.

Ruel J., Lachance G., 2010. Mathematical modeling and experimental testing of three bioreactor configurations based on windkessel models. Heart international 5, e1.

Sun Z., Chaichana T., 2016. A systematic review of computational fluid dynamics in type B aortic dissection. Int J Cardiol 210, 28-31.

Trimarchi S., Tolenaar J.L., Jonker F.H., Murray B., Tsai T.T., Eagle K.A., Rampoldi V., Verhagen H.J., van Herwaarden J.A., Moll F.L., Muhs B.E., Elefteriades J.A., 2013. Importance of false lumen thrombosis in type B aortic dissection prognosis. J Thorac Cardiov Sur 145(3), S208- S212.

Tsai T.T., Evangelista A., Nienaber C.A., Myrmel T., Meinhardt G., Cooper J.V., Smith D.E., Suzuki T., Fattori R., Llovet A., Froehlich J, Hutchison S., Distante A., Sundt T., Beckman J., Januzzi J.L., Isselbacher E.M., Eagle K.A., 2007. Partial Thrombosis of the False Lumen in Patients with Acute Type B Aortic Dissection, New Engl J Med 357(4), 349- 359.

Tse K. M., Chiu P., Lee H.P., Ho P., 2011. Investigation of hemodynamics in the development of dissecting aneurysm within patient-specific dissecting aneurismal aortas using computational fluid dynamics (CFD) simulations. Journal of biomechanics, 44(5), 827-836.

Wan Ab Naim N., Balan Ganesan P., Sun Z., Chee K., Hashim S., Lim E., 2014. A Perspective Review on Numerical Simulations of Hemodynamics in Aortic Dissection. The Scientific World Journal. http://dx.doi.org/10.1155/2014/65252.

Wootton D., Markou C., Hanson S., Ku D., 2001. A mechanistic model of acute platelet accumulation in thrombogenic stenoses. Ann Biomed Eng 29, 321–329.

Xiao N., Alastruey J., Figueroa C.A., 2014. A systematic comparison between 1-D and 3-D hemodynamics in compliant arterial models. International journal for numerical methods in biomedical engineering, 30(2), 204-231.

441 **Figure Captions**

442 **Fig. 1**. Computational models showing locations of inlet and outlets, and (a) inlet flows and
443 predicted outlet flows for (b) TEVAR-P1 and (c) TEVAR-P2. As the BMT model has only one
444 outlet, the predicted outlet flow is equal to the inlet and is therefore not shown.

445

446 **Fig. 2.** Reconstructed model geometries TEVAR-P1, TEVAR-P2 and BMT based on initial CT
447 scans, showing the stented region for TEVAR patients.

448

449 **Fig. 3.** Instantaneous streamlines in the three patient models, calculated at (a) mid-systolic
450 acceleration, (b) peak systole, and (c) mid-deceleration.

451

452 **Fig. 4.** TAWSS distributions in the three patient models: (a) TEVAR-P1, (b) TEVAR-P2, and (c)
453 BMT.

454

455 **Fig. 5.** Evolution of FL surface in TEVAR-P1 following thrombus growth. (a) Reconstructed
456 lumen surface in TEVAR-P1 based on the initial scan, and predicted FL surface following
457 thrombus growth at (b) 7.5 s, (c) 11 s, and (d) 20 s.

458

459 **Fig. 6.** Evolution of FL surface in TEVAR-P2 following thrombus growth. (a) Reconstructed
460 lumen surface based on the initial scan in TEVAR-P2, and predicted FL surface following
461 thrombus growth at (b) 8 s, (c) 20 s, and (d) 42 s, in comparison with the reconstructed
462 lumen surface based on follow-up scans acquired at (e) 1 year, and (f) 4 years after TEVAR.

463

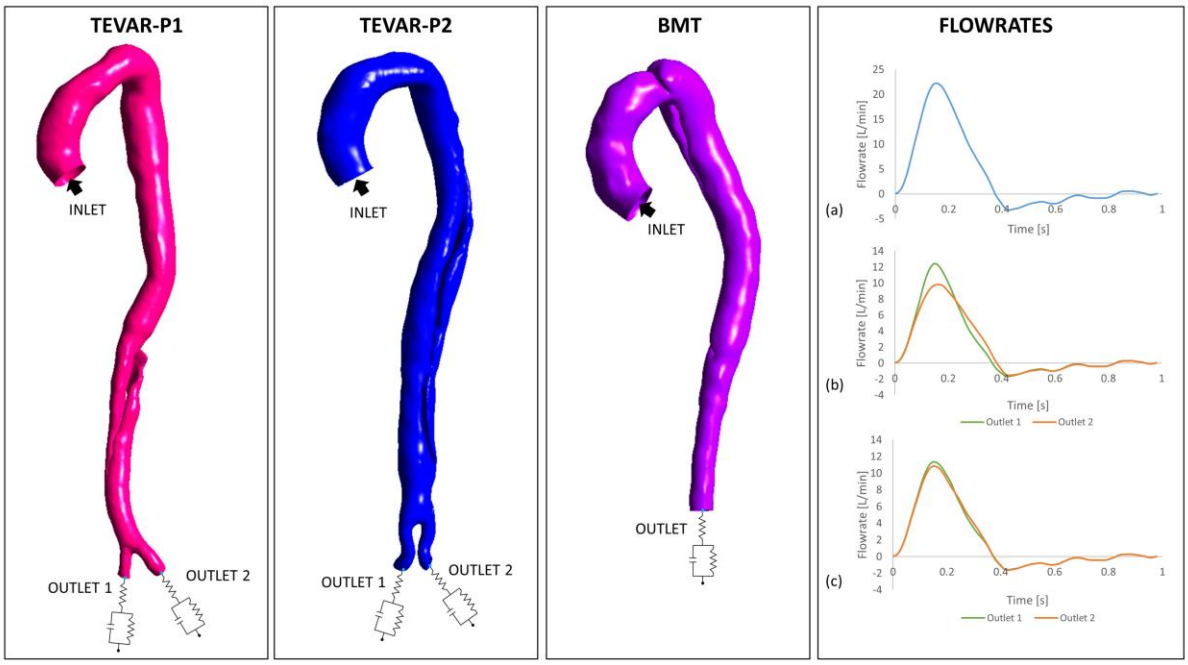

464

465

466 **Fig. 1**. Computational models showing locations of inlet and outlets, and (a) inlet flows and

467 predicted outlet flows for (b) TEVAR-P1 and (c) TEVAR-P2. As the BMT model has only one

468 outlet, the predicted outlet flow is equal to the inlet and is therefore not shown.

469

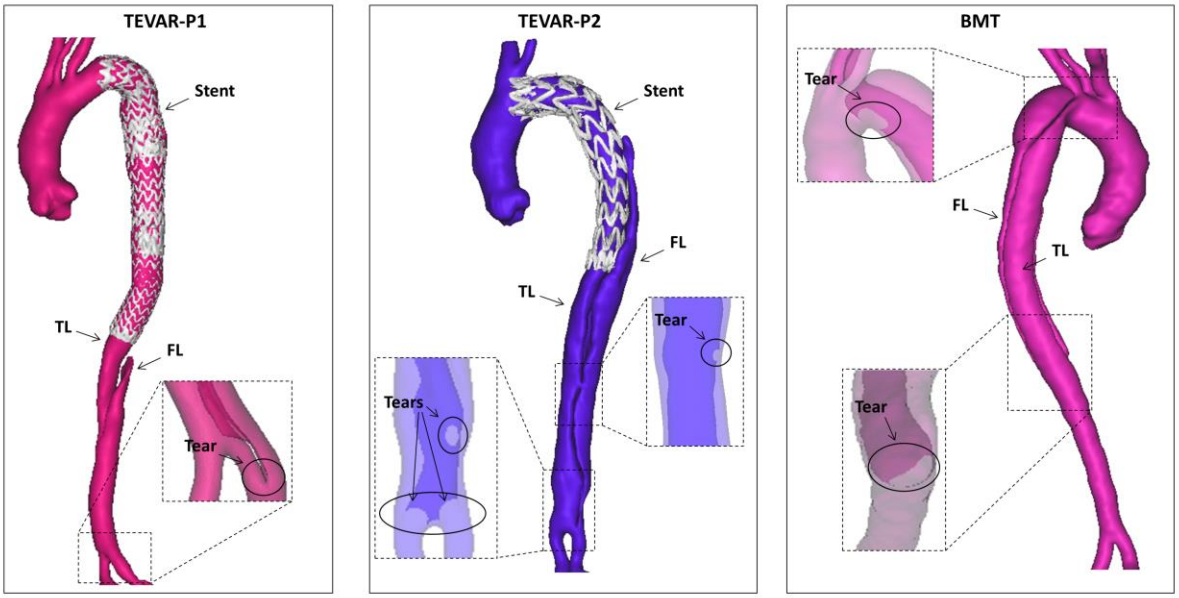

470

471

472 **Fig. 2.** Reconstructed model geometries TEVAR-P1, TEVAR-P2 and BMT based on initial CT

473 scans, showing the stented region for TEVAR patients.

474

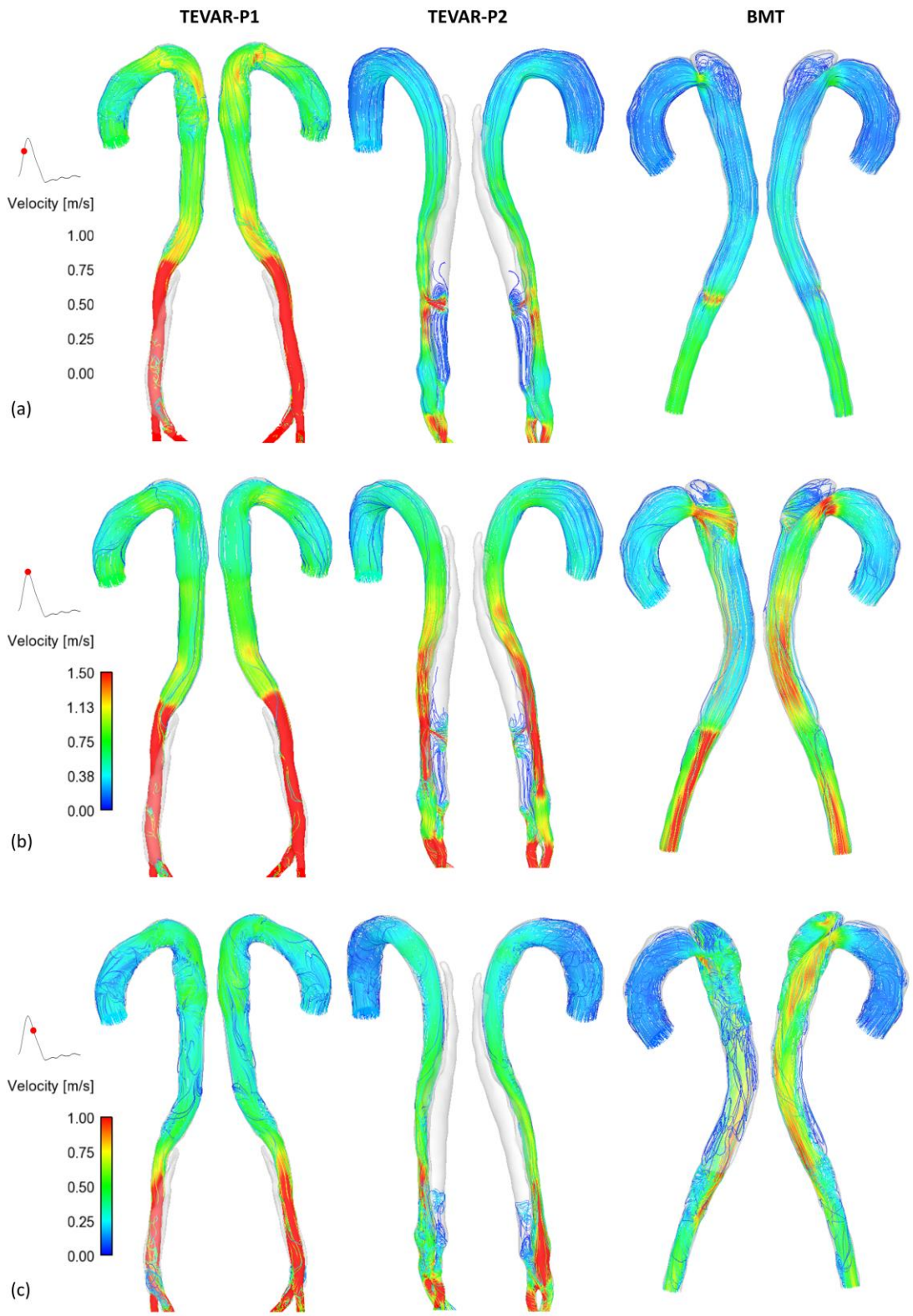

475

476

477 **Fig. 3.** Instantaneous streamlines in the three patient models, calculated at (a) mid-systolic

478 acceleration, (b) peak systole, and (c) mid-deceleration.

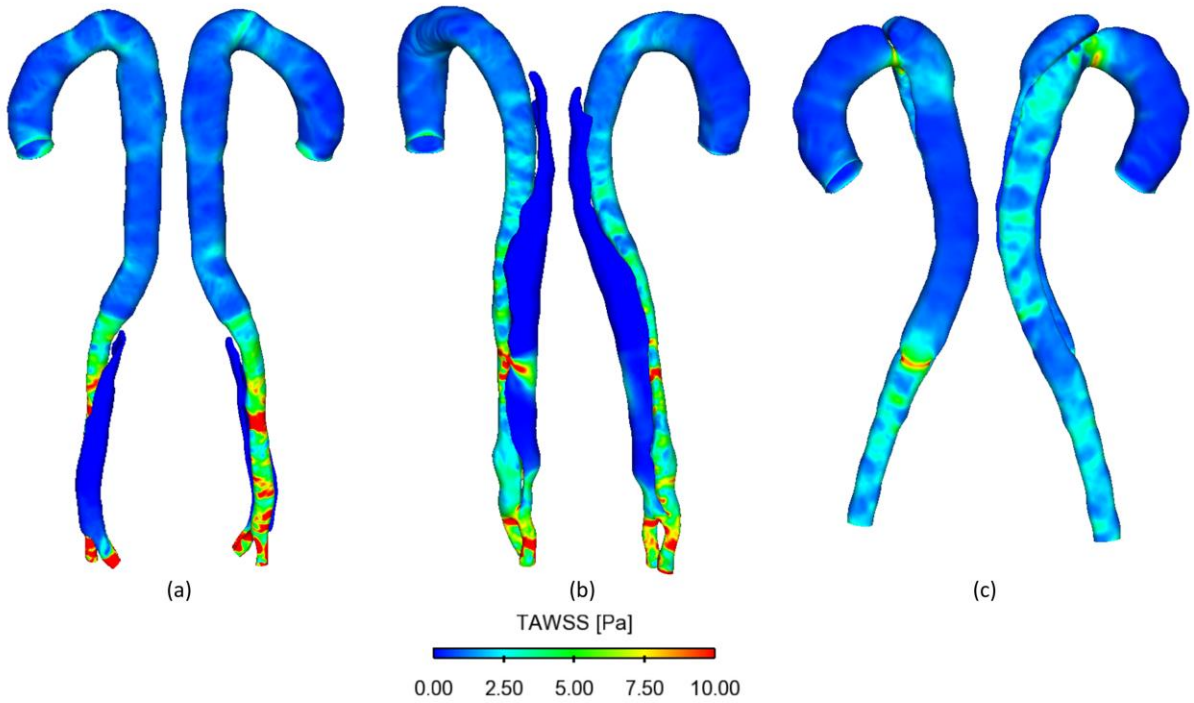

479

480

481 **Fig. 4.** TAWSS distributions in the three patient models: (a) TEVAR-P1, (b) TEVAR-P2, and (c)

482 BMT.

483

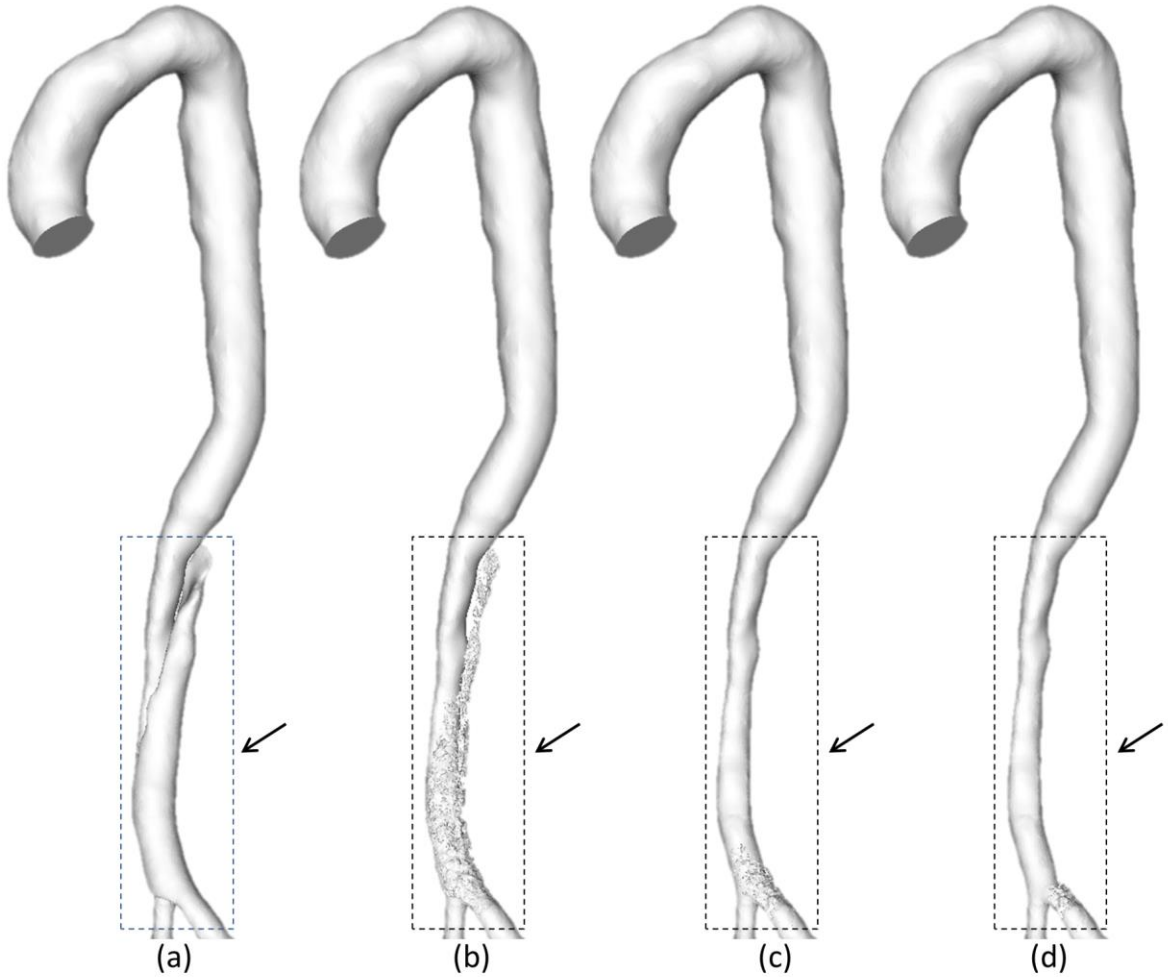

484

485

486 **Fig. 5.** Evolution of FL surface in TEVAR-P1 following thrombus growth. (a) Reconstructed

487 lumen surface in TEVAR-P1 based on the initial scan, and predicted FL surface following

488 thrombus growth at (b) 7.5 s, (c) 11 s, and (d) 20 s.

489

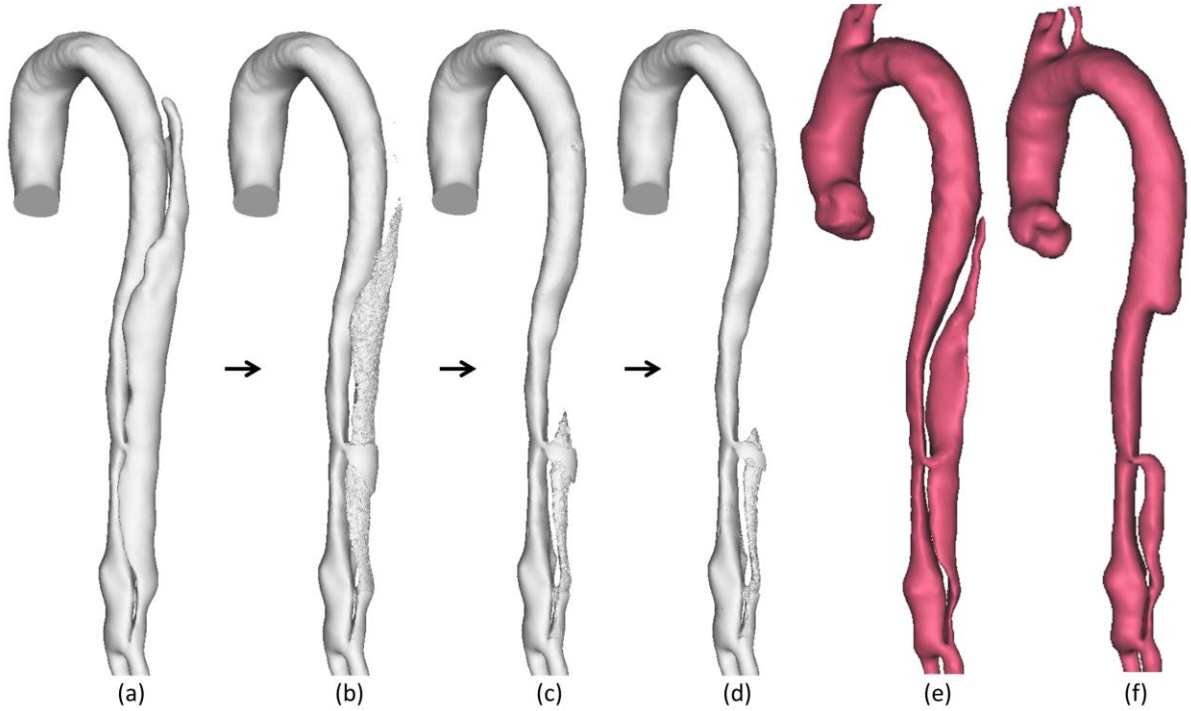

Fig. 6. Evolution of FL surface in TEVAR-P2 following thrombus growth. (a) Reconstructed lumen surface based on the initial scan in TEVAR-P2, and predicted FL surface following thrombus growth at (b) 8 s, (c) 20 s, and (d) 42 s, in comparison with the reconstructed lumen surface based on follow-up scans acquired at (e) 1 year, and (f) 4 years after TEVAR.